

Donut-Shaped Stretchable Kirigami: Enabling Electronics to Integrate with the Deformable Muscle

Yusuke Morikawa, Shota Yamagiwa, Hirohito Sawahata, Rika Numano, Kowa Koida, and Takeshi Kawano*

Electronic devices used to record biological signals are important in neuroscience, brain–machine interfaces, and medical applications. Placing electronic devices below the skin surface and recording the muscle offers accurate and robust electromyography (EMG) recordings. The device stretchability and flexibility must be similar to the tissues to achieve an intimate integration of the electronic device with the biological tissues. However, conventional elastomer-based EMG electrodes have a Young's modulus that is ≈ 20 times higher than that of muscle. In addition, these stretchable devices also have an issue of displacement on the tissue surface, thereby causing some challenges during accurate and robust EMG signal recordings. In general, devices with kirigami design solve the issue of the high Young's modulus of conventional EMG devices. In this study, donut-shaped kirigami bioprobes are proposed to reduce the device displacement on the muscle surface. The fabricated devices are tested on an expanding balloon and they show no significant device (microelectrode) displacement. As the package, the fabricated device is embedded in a dissolvable material-based scaffold for easy-to-use stretchable kirigami device in an animal experiment. Finally, the EMG signal recording capability and stability using the fabricated kirigami device is confirmed in *in vivo* experiments without significant device displacements.

Electronic devices that are used to record biological signals, including signals from the brain (electroencephalogram, electrocorticogram, local field potential/spikes), and other tissues (electrocardiogram, electromyogram [EMG]) are important in neuroscience, brain–machine interfaces, human–machine interfaces, and medical applications. Stretchable electronics enable the integration of electronics for use on soft and curvilinear biological tissues. However, the Young's modulus of elastomer-based conventional stretchable devices is ≈ 20 times higher than that of biological tissues.^[1,2]

Accurate and robust EMG signal recording is necessary in EMG signal-based human–machine interfaces,^[3–5] which allow for prosthesis control in amputated patients. EMG signals can be recorded from the skin surface (surface EMG, sEMG). Wet electrodes made of conductive gel, hydrogel, or sponge saturated with an electrolyte solution and dry electrodes made of noble metals (e.g., gold, platinum, or silver), carbon electrodes, sintered silver or silver chloride

are generally used as the electrodes to record the sEMG signals.^[6] However, the quality of the sEMG signals recorded via such electrodes is affected by the skin surface conditions, such as conductivity and sweating. Sweating attenuates and filters the EMG signals.^[7] In addition, additional layers (e.g., subcutaneous fat and skin) between the signal source and the electrode induce difficulty to separate the signals.^[8] Therefore, some methods of placing the electrode below the skin surface and recording the EMG signals directly from the muscle surface are proposed for achieving stable EMG signal recordings.^[8,9]

Elastomer and hydrogel with high stretchability and small Young's moduli properties are candidate materials of EMG signal recording device.^[10,11] However, the use of elastomer as the device substrate for EMG signal recordings is problematic because these materials have higher Young's moduli [e.g., 730 kPa for polydimethylsiloxane (PDMS)] than muscle and other tissues (e.g., ≈ 1.5 kPa for the brain and 5–40 kPa in resting muscle).^[1,12] In addition, a large deformation of such elastomer-based electronics induces mechanical failure of the device components (e.g., transistors and interconnections) because of the large mechanical mismatch between the


Y. Morikawa, Dr. S. Yamagiwa, Prof. T. Kawano
Department of Electrical and Electronic Information Engineering
Toyoashi University of Technology
1-1 Hibiigaoka Tempaku-cho, Toyohashi, Aichi 441-8580, Japan
E-mail: kawano@ee.tut.ac.jp

Prof. H. Sawahata
National Institute of Technology
Ibaraki College, 866 Nakane, Hitachinaka, Ibaraki 312-8508, Japan

Prof. R. Numano, Prof. K. Koida
Electronics-Interdisciplinary Research Institute (EIRIS)
Toyoashi University of Technology
1-1 Hibiigaoka Tempaku-cho, Toyohashi, Aichi 441-8580, Japan

Prof. R. Numano
Department of Applied Chemistry and Life Science
Toyoashi University of Technology
1-1 Hibiigaoka Tempaku-cho, Toyohashi 441-8580, Japan

Prof. K. Koida
Department of Computer Science and Engineering
Toyoashi University of Technology
1-1 Hibiigaoka Tempaku-cho, Toyohashi 441-8580, Japan

 The ORCID identification number(s) for the author(s) of this article can be found under <https://doi.org/10.1002/adhm.201900939>.

DOI: 10.1002/adhm.201900939

elastomer and these device components.^[13–15] Meanwhile, the hydrogel cannot maintain the robust and conformal contact with the tissues because of dimensional changes in biofluids.^[16] Another issue of such devices in biofluids is that conventional stretchable devices cannot follow the deformation of the wet tissues (e.g., beating heart) because of the wet tissue surface, which results in device (microelectrode) displacement. The displacement of such electrodes on the muscle surfaces should be minimized in the device application to myoelectric pattern recognition-based prosthesis control.^[17]

Low effective modulus comparable to that of biological tissues has been achieved using a kirigami structure (≈ 23 and ≈ 3.6 kPa)^[18] and a mesh structure (≈ 4 kPa).^[19] These two devices exhibit high stretchability under high strain and low effective modulus. They also achieve recording capabilities from the biological tissues. The low effective modulus of these devices enables the minimization of the device-induced physical stress to biological tissues caused by the device placement, compared to conventional elastomer-based stretchable devices (e.g., PDMS).^[2,20,21] Using a stable device material [e.g., parylene

and Styrene-butadiene-styrene,^[18,19] of the above-mentioned devices offer device stability to biofluids. However, kirigami and mesh structures are not able to solve other problems, such as microelectrode displacement over the wet surface of a tissue.^[18]

Figure 1a shows a conventional sheet-type stretchable kirigami bioprobe device^[18] placed on the wet tissue of a muscle. While the muscle contracted, the sheet-type kirigami device slipped over the tissue because of the “no device fixation mechanism” to the target tissue, and the device was not stretched and not followed with the tissue deformation. To overcome the issue of device displacement, here we propose a kirigami bioprobe that can surround the tissue, resulting in the stretching of the device and following tissue deformation (Figure 1b). The proposed kirigami device is fabricated using the approach presented in this work. A 2D donut-shaped kirigami design is implemented, which employs a radially arranged linear array of slits and achieves a low effective modulus (Figure 1c). A photolithography-based 2D microfabrication process of parylene^[22–24] is used to fabricate the 2D donut-kirigami film; this 2D film can be transformed into a 3D cylindrical shape. The donut-shaped

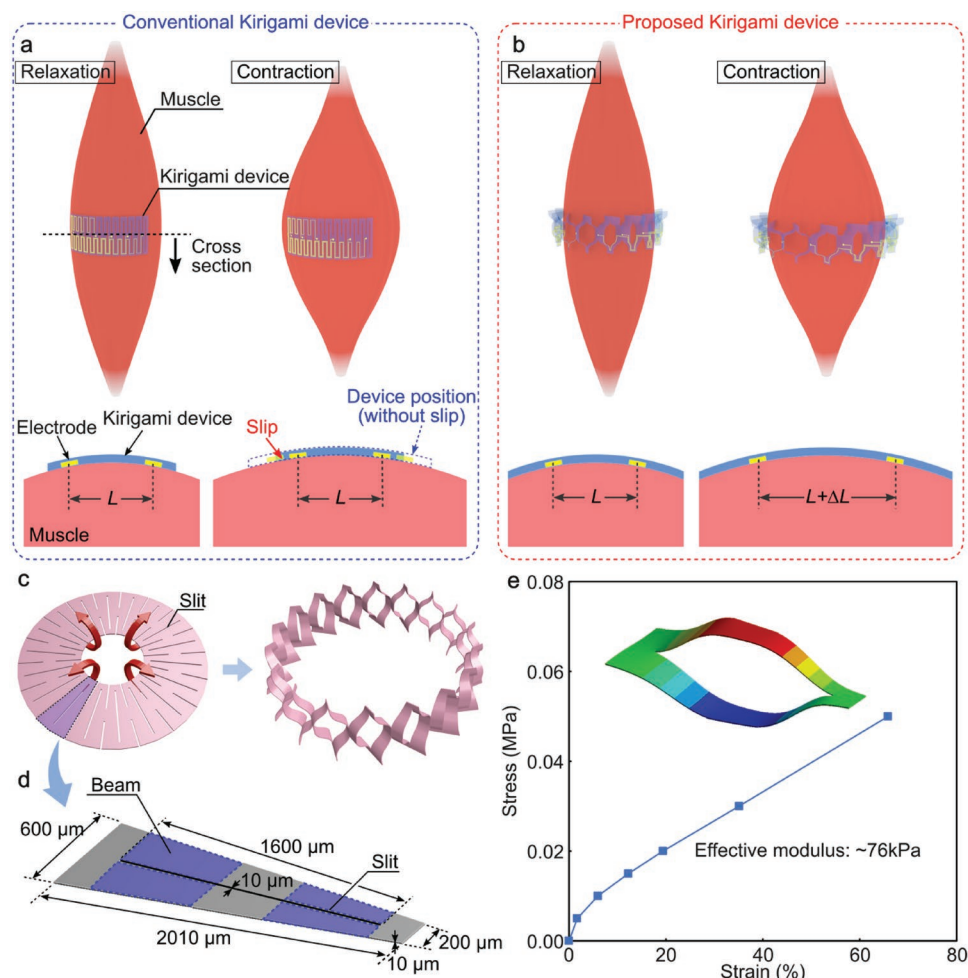


Figure 1. Displacement issue of the conventional kirigami bioprobe device. a,b) Comparison of the devices' displacement over the tissue (muscle) between the conventional sheet-type device a) (left: relaxation, right: contraction) and the proposed kirigami devices b). c) The proposed donut-shaped kirigami device (left: before device transformation from a 2D shape into a 3D shape, right: after transformation). d) One cell model in the donut-shaped kirigami device c) before transformation for the simulation. e) Stress–strain curve of one cell in the kirigami film.

kirigami device realizes the fixation mechanism to the target tissue, and the transformed 3D device geometry is suitable for use in numerous spherically or columnar-shaped deformable biological tissues (e.g., limb and heart). Additionally, an array of microelectrodes is fully integrated with the 3D kirigami device due to the 2D microfabrication process.

Before device fabrication, the stress–strain characteristics of the donut-shaped kirigami device were calculated using the finite-element method. We used the one cell model, which consists of the one slit and four beams around the slit (Figure 1d). In the device design, 26 cells were arrayed in the film along the circle shape (Figure 1c). We used an elastomer parameter of Young’s modulus, which is calculated from the device’s stress–strain curve (Figure 1e). The calculated effective modulus of the donut-shaped kirigami device was 76 kPa, which had a similar order to the Young’s modulus of the resting muscle tissues (5–40 kPa).^[1] The results indicated that the kirigami design causes lower device-induced stress on tissues than that of the elastomer-based stretchable devices (730 kPa for PDMS-device).

On the basis of the simulation, we fabricated donut-shaped kirigami bioprobe devices by using parylene-based microelectromechanical system process^[22–24] (Figure 2a). For device characterization, we designed a single-donut-shaped kirigami device with an array of microelectrodes. We also designed a double-donut-shaped kirigami device, which consists of two arrays of microelectrodes for the multisite EMG signal recording using a mouse’s hind limb.

First, a 5 μm thick parylene-C film was deposited on a silicon (Si) substrate as the device bottom layer. As the device electrode layer, a gold (Au) with titanium (Ti) adhesion layer (total thickness of Au/Ti = ≈ 100 nm) was formed over the bottom layer by sputtering and plasma etchings (argon plasma for Au and CF_4 plasma for Ti). Then, the Au/Ti layer was covered with another parylene layer (5 μm). Both the parylene top/bottom layers were patterned by oxygen (O_2) plasma with a Ti hard mask for creating the kirigami substrate. With this plasma etching process, both electrode sites and bonding pads were also exposed simultaneously. Finally, after the Ti layer was removed (CF_4 plasma),

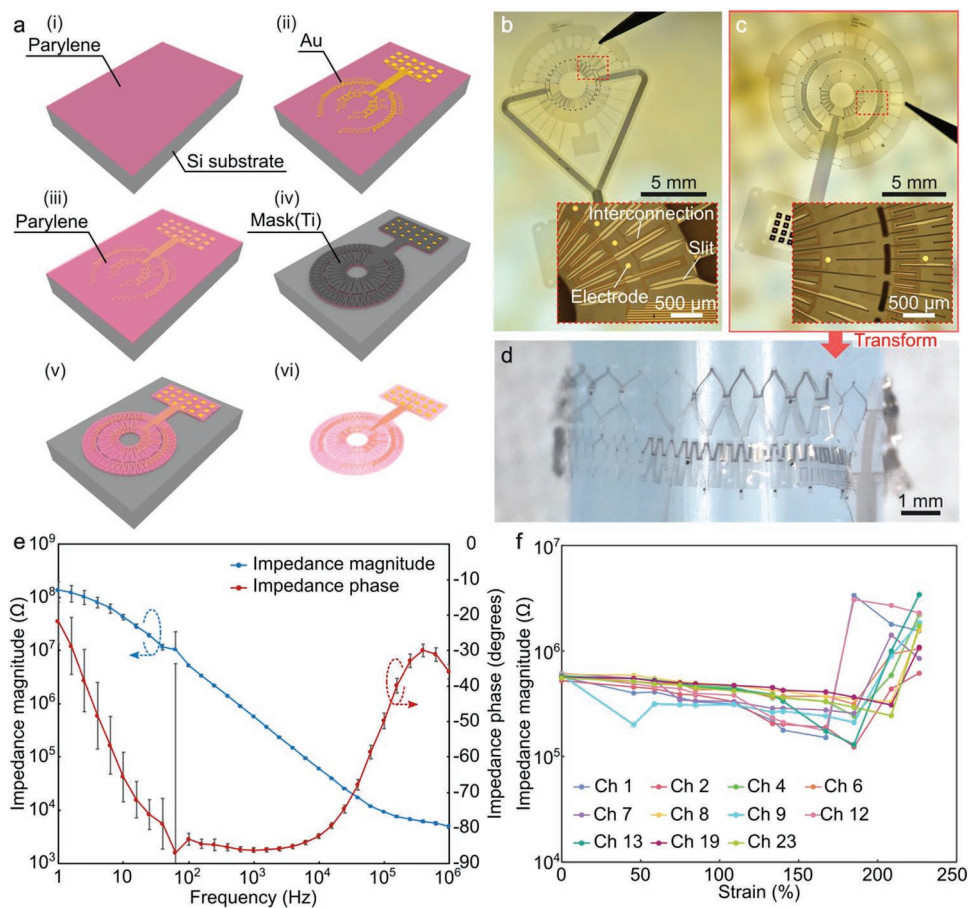


Figure 2. Donut-shaped kirigami bioprobe device. a) Fabrication steps of the donut-shaped kirigami bioprobe device: (i) deposition of first parylene-C as the bottom layer, (ii) patterning of Au electrode layer with Ti adhesion layer, (iii) deposition of the second parylene-C as the top layer, (iv) patterning of both the parylene top/bottom layers, and exposing electrode sites and bonding pads by O_2 plasma with Ti mask, (v) removal of the Ti mask, and (vi) the released kirigami device from the silicon substrate with ethanol. b,c) Photographs showing two kinds of the fabricated donut-shaped kirigami bioprobe devices: single-donut and double-donut shapes. d) Deformed kirigami device with a jig. e) Impedance characteristics of the single-donut shaped fabricated device measured in saline without stretching (0%). Averages and standard deviations of impedance magnitude and phase characteristics are taken from 11 samples (error bars, SD). A deviation of around 60 Hz is due to noise of the measurement system. f) Strain-dependent impedances of the fabricated device (single-donut shape) measured at 1 kHz in saline. Herein, the device stretches from 0% to 226%.

the parylene film was released from the Si substrate by using ethanol.

Figure 2b shows the fabricated, single donut-shaped device with an array of 24-channel Au microelectrodes for the donut kirigami device characterizations. The inner and outer diameters of the donut shape are 2 and 6 mm, respectively, and the film thickness is 10 μm . The length and width of each slit in the film are 1600 and 10 μm , respectively, whereas the slit gap (beam width) ranged from 100 to 300 μm . The fabricated single-donut kirigami with 26 cells has the maximum film's strain of $\approx 175\%$ (calculation). The inset in Figure 2b is the microscope image of the fabricated device, showing 50 μm diameter Au electrodes embedded along the circle shape (4 mm diameter) with a 400 μm interval. Each microelectrode is connected to the bonding-pad through zigzag interconnections. Each slit edge has a circle shape with a 20 μm diameter to prevent the stress concentration confirmed in the previous work.^[18]

Figure 2c shows a double-donut-shaped device for the EMG signal recording. The inner and outer diameters of the inside donut were 2 and 5.6 mm, respectively. The other inner and outer diameters of the outside donut were 5.8 and 8 mm, respectively. The inside donut consisted of an array of 27 cells, whereas the outside consisted of an array of 81 cells. The designed strains inside and outside the donuts were $\approx 185\%$ and $\approx 110\%$, respectively. We experimentally confirmed that the stretchability of the fabricated device exhibited $\approx 200\%$ strain (diameter of 12 mm) for the inside donut. Slit lengths of the inner and the outer donuts were 1500 and 800 μm , respectively. Both the inner and the outer donuts included 10-channel Au microelectrodes with a 50 μm diameter. Intervals of these electrode arrays were 1200 and 2200 μm , respectively, and the interval between the inner and outer electrodes was 1600 μm . Figure 2d shows the transformation of the fabricated device from a 2D donut shape to the 3D cylindrical shape using a jig.

Electrolyte/metal interfacial impedance magnitude of the embedded Au microelectrode of single-donut-shaped kirigami device was measured in saline solution. The magnitude of Au microelectrode's impedance without stretching the device (stretchability = 0%) was $\approx 576 \text{ k}\Omega$ at 1 kHz (Figure 2e). The impedance magnitude is low enough to measure biological signals.^[25] Figure 2f shows the strain-dependent impedance characteristics of Au microelectrodes in the single-donut-shaped kirigami device. At the strain range of 0–100%, no significant changes in the impedance were observed because the film in this condition is deformed by the beam's bending itself, and no significant stress was concentrated in the film. At strain ranges of $>100\%$, the value of the impedance initially decreased but then increased due to the film breaking. Under this condition, strain-induced stress was concentrated at the slit's edge until it reached its limit. This stress concentration caused both issues of the peel off of parylene bi-layer and the crack at the slit edge (Figure S1, Supporting Information). The parylene peeling off caused the exposure of the Au-interconnections in the saline solution; the value of the device impedance decreased, since the area exposed to the saline solution was increased. When the cracks extended and reached the interconnections, the value of the device impedance increased due to the film breaking and the disconnection of the interconnections.

To confirm the device's deformability on the expanding biological tissue, we conducted displacement tests of the fabricated donut-shaped kirigami device on a balloon (Figure 3b, and Movie S1, Supporting Information). In this test, we also used conventional sheet-type kirigami device for comparisons (Figure 3c, and Movie S1, Supporting Information). Both donut-shaped and sheet-type kirigami devices had the same slit length of 1600 μm . These devices adhered to the balloon by water between the device and the balloon surfaces. The device had markers on its surfaces such that we can determine the perpendicular distance from the center line on the balloon. The side and cross sectional views of the balloon before and after the expansion are shown in Figure 3a. Considering the curvature of the balloon surface, the device displacement was defined as the length between the calculated and measured marker positions on the balloon's surface after the balloon's expansion. The device displacement is defined as follows

$$\Delta L = \frac{D_1 |\theta_1 - \theta_0|}{2} \quad (1)$$

$$\theta_0 = \sin^{-1} \frac{2L_0}{D_0} \quad (2)$$

$$\theta_1 = \sin^{-1} \frac{2L_1}{D_1} \quad (3)$$

In these equations, L_0 and L_1 are the marker distances from the balloon's center before and after the expansion, D_0 and D_1 are the diameters of the balloon before and after the expansion, and θ_0 and θ_1 are the angles of balloon's markers before and after the expansion, respectively (Figure 3a).

Figure 3d shows the device displacement curves taken from three trials of the balloon expansion using the same donut-shaped kirigami device (each trial has five strain cycles of the explanation). Each curve represents the averages and standard deviations taken from the five strain cycles in the trial. Herein, the balloon was expanded to the strain of $\approx 50\%$, which is five times larger than the reported muscle strain of human tibialis anterior muscle ($\approx 10\%$ strain at maximum contraction intensity).^[26] The donut-shaped kirigami device showed that the device followed the expansion of the balloon with the displacement of $<0.2 \text{ mm}$ at the balloon's expansion of $\approx 50\%$. Meanwhile, the sheet-type device cannot follow the expansion of the balloon because of the displacement (Figure 3e). The displacement of the sheet-type device was $>1.5 \text{ mm}$, while the balloon expanded to $\approx 50\%$. Figure 3f depicts these displacements for comparisons (each point is averaged from the three trials in Figure 3d,e). The displacement of the donut-shaped device was ≈ 8 times smaller than that of the sheet-type device.

Figure 4a–d shows the repeated strain test of the donut-shaped and sheet-type kirigami devices. The cycles of the balloon expansion were 100 (Movie S2, Supporting Information). The displacement is defined as the difference in distance between the initial marker position on the expanded balloon surface [Marker (Cycle 1), Figure 4b] and the marker position in the following cycles [Marker (Cycle n), Figure 4b]. Figure 4e,f illustrates the cycle-dependent displacement of the lateral (x-axis) and perpendicular (y-axis) directions against the

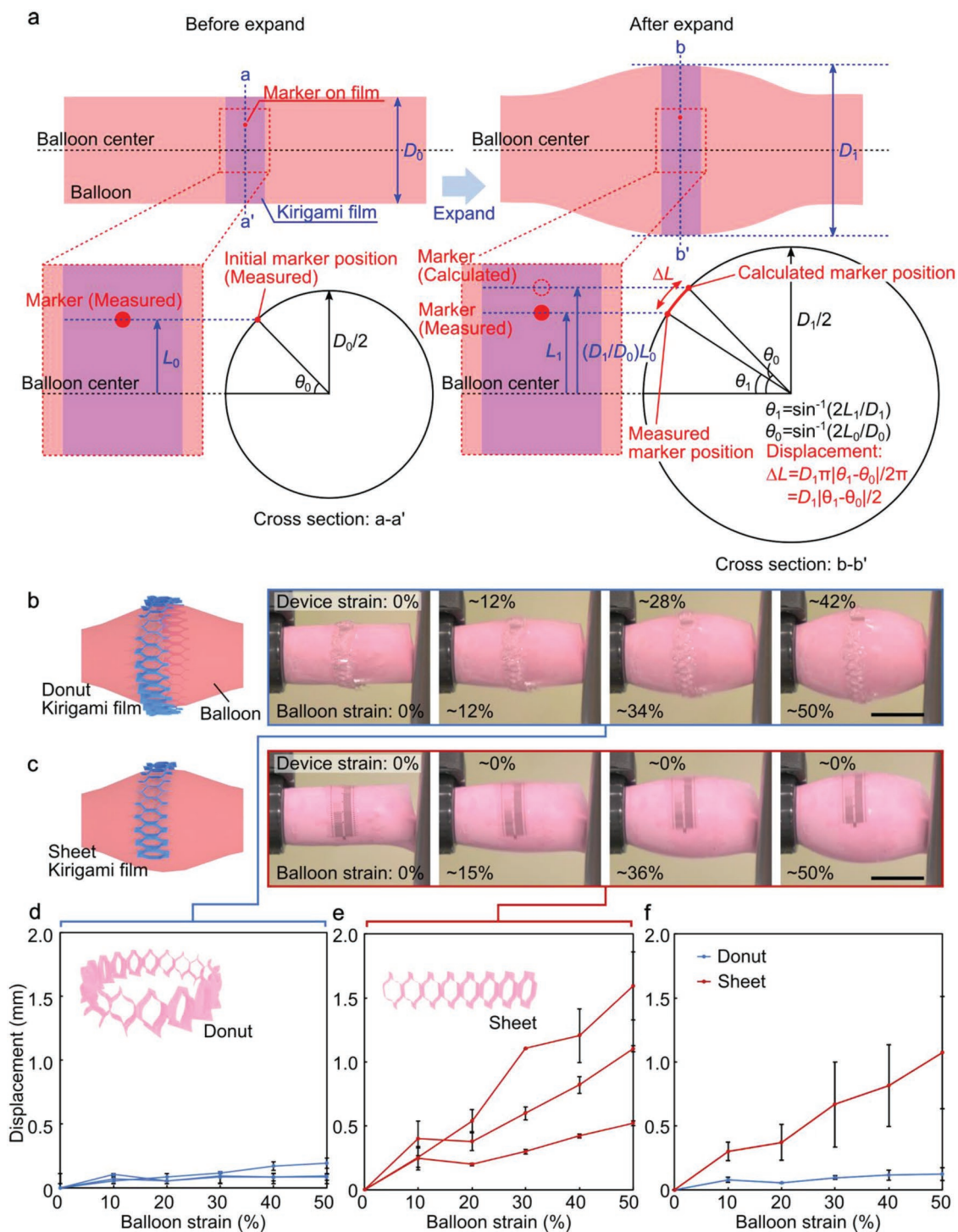


Figure 3. Displacement test of kirigami device on balloon surface. a) Schematics of the displacement test before and after balloon expansion. b,c) Photographs showing deformations of fabricated donut-shaped b) and sheet-type device c) while the balloon expands from 0% to 50%. Scale bars = 5 mm. d,e) Marker displacement of the donut-shaped and sheet-type devices depending on the strain on the balloon surface. Each curve is taken from the three trials of the balloon expansion, and represents the averages (five strain cycles in the trial). Error bars: SD. f) Averaged marker displacement for the donut-shaped and sheet-type devices taken from the three trials in d) and e). Error bars: SD.

balloon center line. The donut-shaped device showed that the displacement gradually increased as the cycle number increased (Figure 4c,e,f). Meanwhile, the displacement of the sheet-type

device significantly increased as the trial number increased (Figure 4d–f). The device moved downward and disappeared from the camera view at the cycle range of over 50 cycles

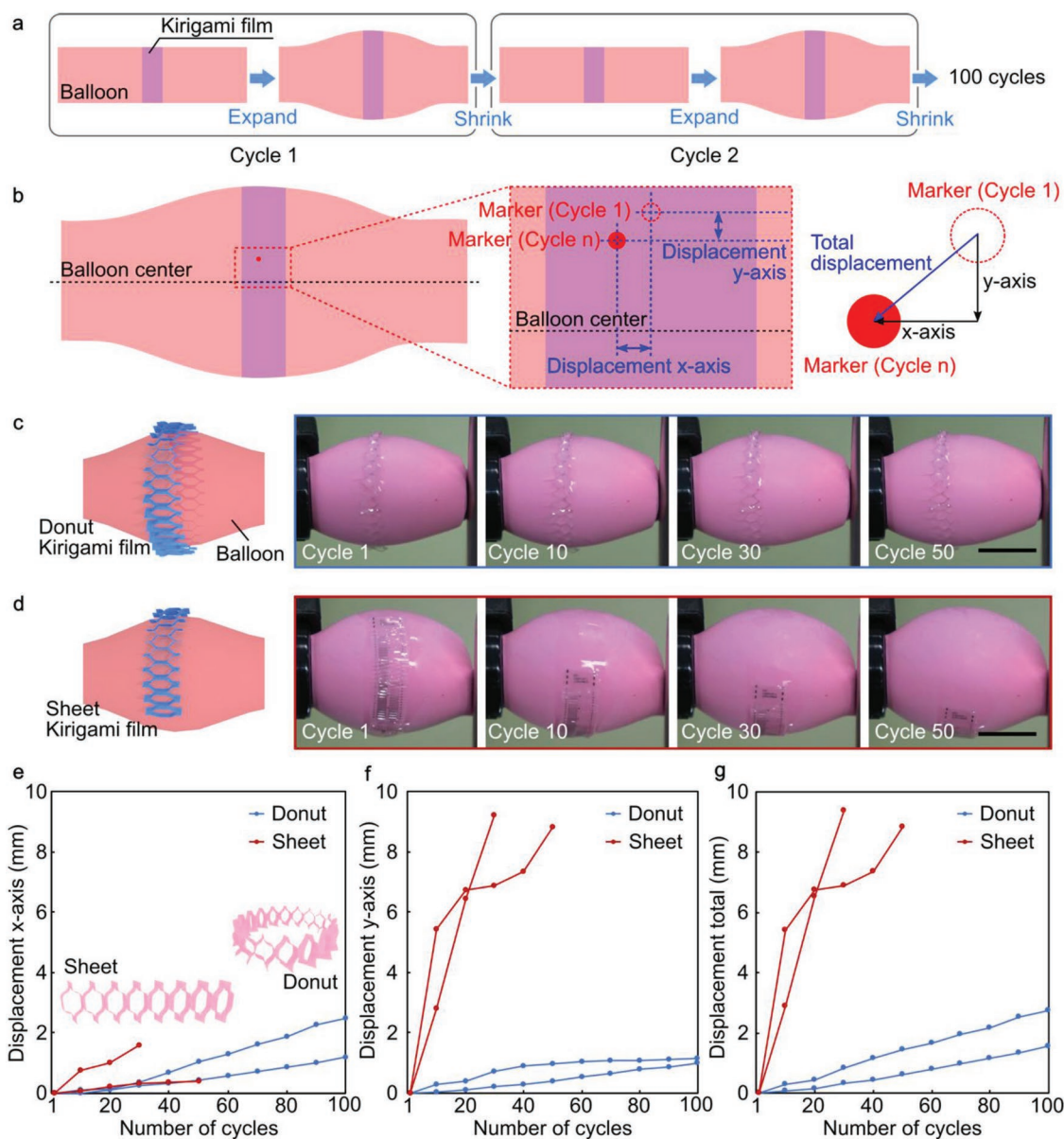


Figure 4. Repetition of displacement test of kirigami device on the balloon surface. a) Schematics of the device on the surface of a balloon, which expands and shrinks repeatedly. b) Schematics of the distance between the initial marker position on the expanded balloon surface [Marker (Cycle 1)] and the marker position in the following cycles [Marker (Cycle n)]. c, d) Photographs showing the deformations of the donut-shaped c) and sheet-type d) devices while repeating the balloon expansions for 50 cycles. Scale bars = 5 mm. e, f) Marker displacements of the x e) and y f) axes for the donut-shaped and sheet-type devices depending on the balloon expansion cycles. Each curve is taken from the two trials of the balloon expansion (each trial has 100 cycles of strain). g) Total marker displacement taken from the displacements of each direction [x e) and y f) axes] for the donut-shaped and sheet-type devices.

(“Cycle 50,” in Figure 4d). Figure 4g shows the total displacements calculated with the displacements along the x and y axes (Figure 4b). The total displacement of the donut-shaped device was at least five times smaller than that of the sheet-type device. Although, the donut-shaped device showed some displacement on the balloon, the device follows the balloon’s expansion without significant slipping or peeling off. The experimentally measured device displacements (Figures 3d–f and 4e–g) were normalized to the diameter of the balloon, where each device was placed (along the x-axis, as shown in Figure 4b).

In animal experiments, handling such thin-film devices is problematic because the film geometry (<10 μm in thickness) is not sufficiently self-supporting to be manipulated.^[27] In addition, kirigami device is more flexible and stretchable compared to the thin-film devices without slit patterns. To overcome the difficulty of the handling of kirigami devices in animal experiments, the fabricated kirigami device was embedded in a cylinder of polyethylene glycol (PEG), which is a biocompatible and soluble material (melted by heating and dissolved with liquid) (Figure 5a).

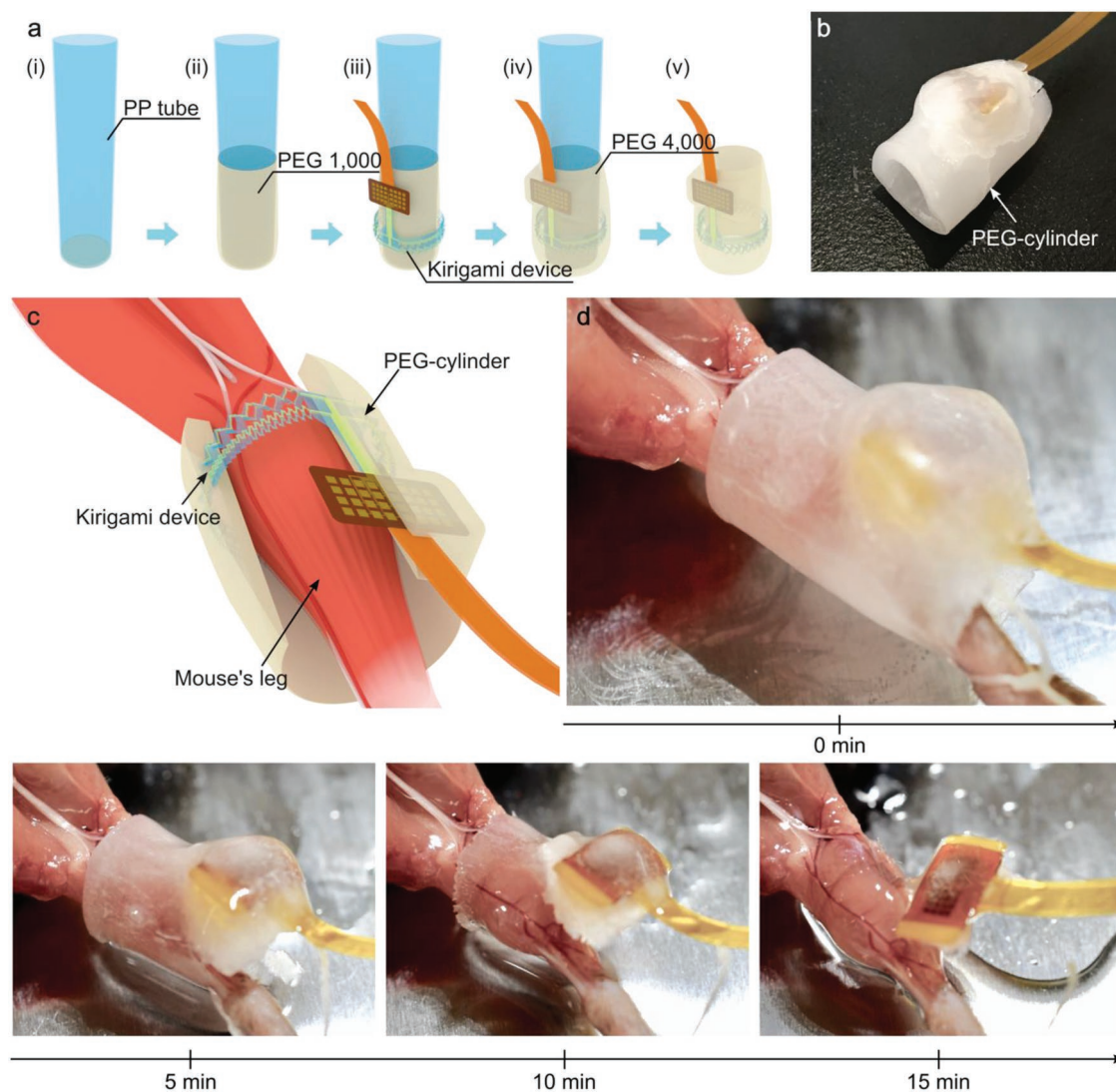


Figure 5. Device package with cylindrical PEG scaffold. a) Process steps of the PEG scaffold: (i,ii) coating PEG 1000 as the sacrificial layer on a low-temperature PP tube (iced water in the PP tube), (iii) attaching donut-shaped kirigami device to the PEG layer, (iv) coating PEG 4000 as the scaffold layer over both the kirigami device and the sacrificial layer, and (v) releasing of the kirigami device with the PEG scaffold from the PP tube by melting the sacrificial layer (PEG 1000) with PP tube heating (hot water in the PP tube). b) Photograph of the kirigami device embedded in PEG scaffold. c,d) Schematic and photographs showing the PEG-scaffold-embedded kirigami device attached to a mouse's hind limb. PEG scaffold is dissolved by dropping saline solution, and the kirigami device is exposed from the PEG within ≈ 15 min.

The fabricated device was successfully embedded into the PEG cylinder. This procedure is described in Figure S2 (Supporting Information). During device embedding, PEG 4000 and PEG 1000 with different melting characteristics were used for the scaffold and the sacrificial layers, respectively. First, melted PEG 1000 was coated as the sacrificial layer on a low-temperature polypropylene (PP) tube (iced water in the PP tube) with one side closed. Then, the kirigami device was stretched and transformed into cylindrical shape, and the device was surrounded with the sacrificial layer (PEG 1000) (Figure 5a). Second, PEG 4000, as the scaffold layer, was coated over both the device and the sacrificial layer. Finally, the fabricated device with the scaffold layer of PEG 4000 was released from the PP tube by melting the sacrificial layer with heating (hot water in the PP tube).

Figure 5b shows the PEG-cylinder-embedded kirigami device. The inner diameter of the PEG-cylinder is ≈ 8 mm and the thickness is ≈ 1 mm. To confirm the dissolving property of the PEG cylinder, we conducted the dissolving test using a mouse's hind limb *in vivo* (Figure 5c,d). As the result, the PEG cylinder was dissolved by dropping saline solution, and the kirigami device was exposed from the PEG cylinder within ≈ 15 min. After dissolving the PEG cylinder, we confirmed the conformal wrapping of the fabricated kirigami device around the mouse's hind limb.

The recording capability of the donut-shaped kirigami device was confirmed using an anesthetized mouse. The fabricated device embedded in the PEG cylinder was placed on the muscle of the mouse's hind limb by dissolving the PEG with saline solution (Figure 5d). After dissolving the PEG,

the kirigami device was wrapped around the leg muscles (Figure 6a–c).

These electrodes were placed on the muscles, whereas the Ch.4 and Ch.9 electrodes in the array were positioned over the tibialis anterior (TA) and medial gastrocnemius (MG) muscles, respectively (Figure 6d). The recorded signal via the electrode in Ch.9 during the nerve stimulation with a biphasic square wave (1 ms duration, 2 s inter trial interval, inset in Figure 6e) is presented in Figure 6e. The stimulation intensity ranged from 320 to 1020 mV_{pp}. The threshold voltage, T , was identified as the stimulation intensity at which the smallest EMG response was observed in Figure 6e.

The previous studies proved that nerve stimulation causes the muscle response, passing through afferent fiber, spinal cord, efferent fiber, and neuromuscular junction.^[28] Thus, the

latency of the EMG signals can be obtained by calculating conductive velocities of the afferent and efferent fibers and synaptic delays of spinal cord and neuromuscular junction. Positions of the stimulated area of nerve and recorded area (electrode position) also dominate the latency. The conductive velocity for sural nerve and peroneal nerve is in the range of 40–50 m s⁻¹, and the synaptic delays are ≈1 ms for spinal cord and ≈0.75 ms for neuromuscular junction. Distances from the stimulated area to spinal cord and from the spinal cord to the neuromuscular junction were 18 and 24 mm, respectively. According to these values, the latency of EMG signal response to the nerve stimulation is calculated to be in the range of 2.6–2.8 ms.^[29–31] EMG cannot be clearly distinguished from the end point of the stimulation-induced artifact in this range. Therefore, to clearly distinguish the EMG from the artifact, we used waveforms

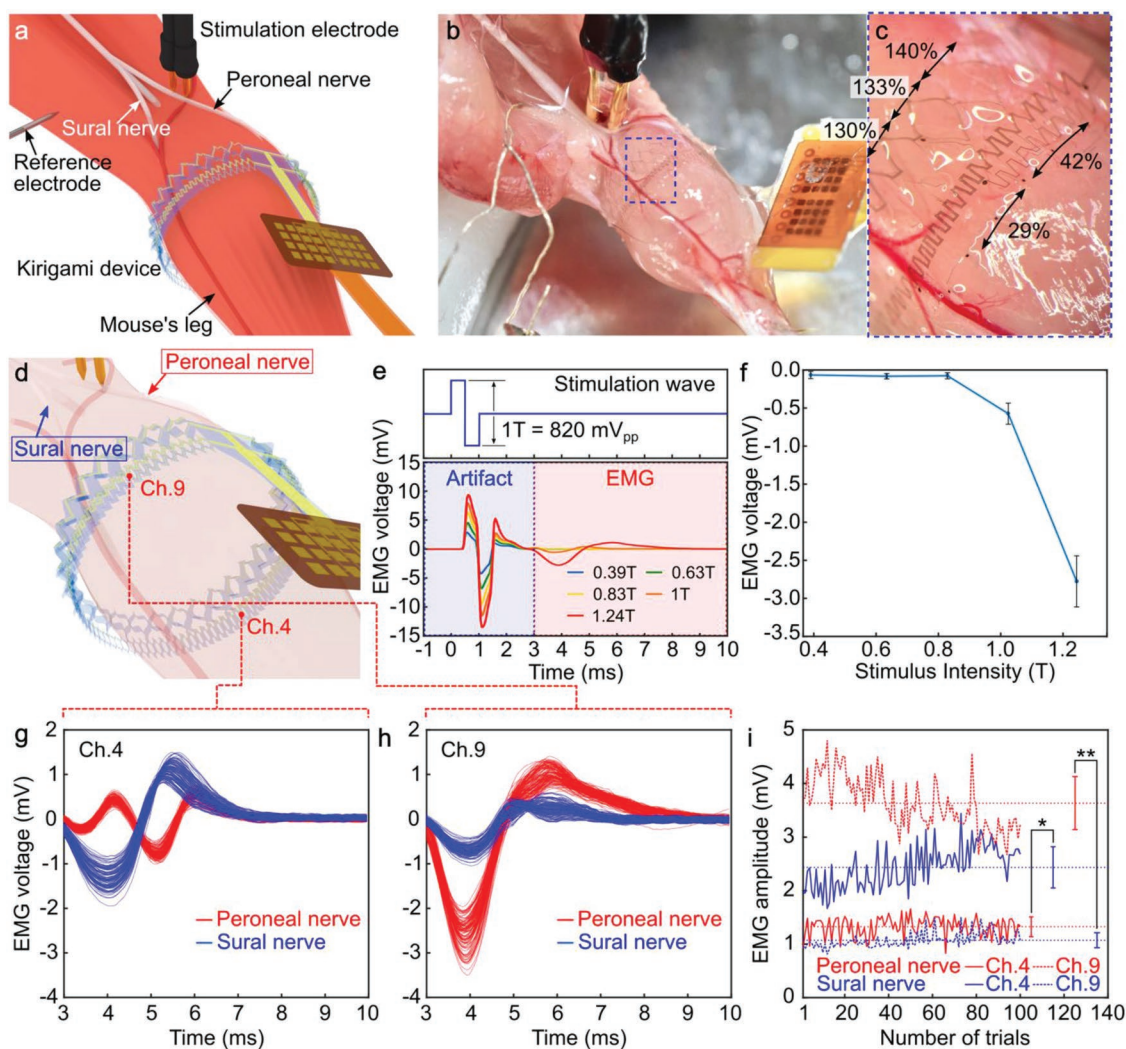


Figure 6. EMG signal recording from a mouse's hind limb in vivo. a–c) Schematic and photographs showing donut-shaped kirigami device wrapped around a mouse's hind limb. d) Schematic showing positions of two electrodes during the EMG signal recording. Electrodes Ch.4 and Ch.9, which are placed on opposite to each other on a mouse's hind limb, stimulating the two branches of the sciatic nerve, namely, the peroneal and sural nerves. e) Recorded signals via an electrode Ch.9 in the device during the nerve stimulations. Amplitudes of the stimulation range from 320 to 1020 mV_{pp} (stimulus intensity of 0.39T–1.24T). f) Stimulus intensity-dependent EMG signal amplitudes. g,h) Recorded EMG signals via the two electrodes (Ch.4 and Ch.9). i) Peak-to-peak amplitudes of the recorded EMG signals. Horizontal dashed lines represent averages for each EMG signal amplitude. The error bars, SD (*: $p = 1.37 \times 10^{-65}$, **: $p = 1.40 \times 10^{-114}$, Student's *t*-test; $df = 198$).

3 ms after the nerve stimulation. According to this criterion, the negative peak amplitude of EMG signal was calculated from the signal during time range of 3–10 ms from stimulation onset.

Figure 6f shows negative peak amplitudes of recorded EMG signals (3–10 ms), depending on the stimulus intensity. No increases in the EMG signal amplitude were observed with the stimulation voltages of 320–680 mV_{pp} (stimulus intensity of 0.39T–0.83T). However, the EMG signal amplitude increased with the stimulation voltage of >680 mV_{pp}. The nonlinearities observed between EMG and stimulation voltages suggest that the recorded signals were originated from physiological response rather than the artifact.^[32,33]

Figure 6g,h shows the recorded EMG signals (100 trials) through the Ch.4 and Ch.9 electrodes while stimulating to the two branches of sciatic nerve, namely, the peroneal and sural nerves (Figure 6a). These electrodes, which were placed at opposite sides of the leg, were positioned over the TA and MG muscles, respectively. Figure 6i shows the peak-to-peak amplitudes of recorded EMG signals via two electrodes of Chs.4 and 9, while stimulating to two branches of sciatic nerves. Student's *t*-test was used to analyze the statistical differences between the EMG signals evoked by either peroneal or sural nerve stimulation. The effect of those stimuli was statistically significant on recorded signals via each electrode [Student's *t*-test; *df* = 198, *p* = 1.37×10^{-65} (Ch.4), *p* = 1.40×10^{-114} (Ch.9)]. These EMG signals were also observed using a conventional electrode with a 1 mm diameter made of Au (Figure S3, Supporting Information). In addition, the displacement of the device was recorded to be <0.1 mm after the 20 nerve stimulation trials, as confirmed in the movies and pictures taken from the animal experiment (Figure S4 and Movies S3 and S4, Supporting Information).

To achieve accurate and robust EMG signal recordings, microelectrode displacement while the muscle stretches should be minimized. The kirigami-based bioprobe device, which has advantages of high stretchability and the device-induced less tissue stress, helps to achieve intimate tissue integration of the device. In addition, the proposed donut shape of the kirigami device solves the issues of device displacement over the muscle. This issue has not been solved by both the conventional sheet-type kirigami device and various stretchable devices that are based on the elastomer and hydrogel materials.

The effective modulus of the fabricated donut-shaped kirigami device of 76 kPa was a similar order to the Young's modulus of the resting muscle tissues of 5–40 kPa. However, the effective modulus of the kirigami device was still larger than that of the muscle and the other tissues (e.g., ≈1.5 kPa for the brain).^[1,12] The effective modulus of the kirigami device can further be decreased by changing in the dimensions of each beam (or slit)^[18] and change the material used to make the device. The candidate soft materials for the kirigami structure include PDMS^[34] and Ecoflex.^[35]

A stretchable kirigami device is based on the 3D deformation of each beam. Therefore, it is necessary to discuss the effect of this device's roughness on the smooth surface of a biological tissue. An issue, which is associated with the 3D deformation, is that the sharp edge of the tilted beam causes tissue stress. However, tissue damage was not observed when the kirigami device was applied to the hind limb of a mouse (Figure 6c). This process was repeated for 100 trials and the EMG signal

was recorded. Moreover, no damage or tissue (e.g., mouse's brain and heart tissues) malfunction was observed during the signal recording. This was demonstrated in a previous work.^[18] However, the long-term device implantation could cause some tissue damage. The tissue stress associated with the sharp kirigami's edge can also be decreased using a device material with the small Young's modulus (e.g., PDMS^[34] and Ecoflex^[35]) than that of the parylene (2.8 GPa). The beam's tilt also makes insufficient contact of each electrode to the tissue surface, degrading the quality of the recording from the muscle. The electrode contact is improved by the additional device design around the electrodes. In terms of the curb of the out-of-plane deformation of the kirigami structure, some studies proposed the kirigami design with the in-plane-deformation.^[35,36]

We also demonstrated the recording capability of the kirigami device by using a mouse's hind limb. The results indicate that the donut-shaped kirigami device has the capability to record the EMG signals and distinguish the responses evoked by stimuli for different nerves. We also confirmed that not only the donut-shaped kirigami device was unaffected by the muscle deformation, but also that it did not affect the muscle function, such as the disturbing the muscle's deformation and causing an ischemia. The device's displacement of <0.1 mm, which was confirmed in the animal experiment, has the same order as the diameter of muscle fibers (e.g., ≈50 μm in gastrocnemius muscles^[37]). This indicates that the donut-shaped kirigami device realizes small enough device's displacement on the muscle for the stable recording of the EMG signals. In the analysis of the EMG signal recording, the EMG signal is defined in the range of 3–10 ms (Figure 6e). This range is used for the detection of the response caused by the nerve stimulation propagating to the direction of the afferent and through the spinal cord (H-reflex). The response caused by the stimulation propagated to the direction of the efferent (M-wave) can be observed in ≈1 ms. This response could not be distinguished in this analysis due to presence of the artifact. However, the effect of the artifact associated with the electrical stimulations can be ignored for practical applications.

We used an Au microelectrode that had an impedance of ≈576 kΩ at 1 kHz (50 μm in diameter). It should be noted that the kirigami device can also be used for muscle stimulation with an electrode material with lower impedance and higher charge injection characteristics compared to Au [e.g., platinum, platinum black, iridium oxide, iridium oxide/platinum black,^[38] poly(3,4-ethylenedioxythiophene)^[39]]. Such kirigami devices with stimulating electrodes will help in achieving individual stimulation of muscles, offering an application to treating paralyzed patients.^[40]

The kirigami bioprobe with its 3D cylindrical shape enables the fixation of the device's microelectrodes to the target muscles, thereby solving the issue of device displacement. The difficulty of handling the cylindrical and flexible kirigami device during its attachment to the mouse's hind limb was overcome, using a PEG scaffold (Figure 5). The PEG scaffold is also applicable to different shapes and sizes of organs and tissues, by varying the shape of PEG before the device attachment (Figure 5a(iii)). The diameter and stretchability (effective modulus) of the kirigami bioprobe can also be varied by changing the slit design, depending on the target tissues and

organs. Although the application of the device is limited to tissues and organs with open ends, as demonstrated in the case of the mouse's limb, the device is also applicable to legs, arms, fingers, abdomen, back, heart, and others.

In the future research, we plan on implanting the kirigami device in a mouse to confirm the long-term recording capability of the device. Additional layers (e.g., skin and fat) will be placed over the device during the kirigami device implantation on the muscle surface. In such a condition, the out-of-plane deformation of the kirigami device is confined by these additional layers, and the stretchability of the kirigami device might be affected. However, we confirm that the kirigami device still maintains its stretchability under this condition, in which the kirigami has another layer as the device implantation (Figures S5 and S6, Supporting Information). The durability of the kirigami device is required for the long-term implantation, and the kirigami structure is not fractured. Moreover, plastic deformation is not observed in the 1000 cycling load test with a strain of $\approx 200\%$ (Figure S7, Supporting Information).

For device implantation, minimizing the device package is necessary. As we demonstrated in in vivo EMG signal recording by using a mouse's hind limb, the kirigami device was electrically connected to flexible printed circuits (FPC) with epoxy by hand. The geometry of the terminal between the parylene-kirigami and FPC was $5 \times 8 \text{ mm}^2$. Implantation of a device of this size is impossible in mice. A way to minimize the device package is by flip-chip bonding technique. The use of wireless technology with the kirigami device will be required to further minimize the invasiveness for long-term applications.^[41]

In this study, we proposed donut-shaped kirigami bioprobe devices for accurate and robust EMG signal recording unaffected by muscle deformation. The kirigami device decreased the device-induced tissue stress. This was confirmed in a simulation that showed that the strain–stress of the kirigami device is ≈ 10 times smaller than that of the conventional elastomer-based stretchable film. The donut shape allows the kirigami device to be wrapped around the muscle and to follow muscle deformation without significant device displacement over the muscle. Embedding the kirigami device in a dissolvable material of PEG solved the difficulty of using the flexible, stretchable, and thin-film kirigami device in an animal experiment. In vivo signal recording using a mouse's hind limb confirmed EMG signal recording capability without significant electrodes displacement to produce a stable EMG signal recording unaffected by muscle deformation.

The advantages of the proposed device (low effective modulus, high strain, and easy fixation to deformable tissues) offers stable EMG signal recording in the long-term and chronic applications, although the animal experiment presented in this paper demonstrated the device's acute recording capability using the mouse's hind limb. In addition to these advantages, the proposed donut-shaped kirigami approach allows the integration of an array of dense microelectrodes with the flexible and stretchable device film within the 3D cylindrical shape. The device's electrodes enable the acquisition of high-spatiotemporal EMG signals from the target muscle. The proposed device can be used in numerous applications, such as human–machine interface and muscle activity mapping in free moving, which have not been achieved by other electrode devices.

Experimental Section

All experimental procedures using animals were approved by the committees for the use of animals at Toyohashi University of Technology, and all animal care followed the Standards Relation to the Care and Management of Experimental Animals (Notification No. 6, March 27, 1980 of the Prime Minister's Office of Japan).

Supporting Information

Supporting Information is available from the Wiley Online Library or from the author.

Acknowledgements

This work was supported by Grants-in-Aid for Scientific Research (B) (Nos. 17H03250 and 16H05434), for Young Scientists (A) (No. 26709024), on Innovative Areas (Research in a proposed research area) (No. 15H05917), and Strategic Advancement of Multi-Purpose Ultra-Human Robot and Artificial Intelligence Technologies program from NEDO. Y.M. was supported by the Leading Graduate School Program R03 of MEXT. R.N. was supported by Takeda Science Foundation. K.K. was supported by Toyota Physical & Chemical Research Institute Scholars.

Conflict of Interest

The authors declare no conflict of interest.

Keywords

electromyography, kirigami, stretchable devices

Received: July 17, 2019

Revised: October 5, 2019

Published online: November 7, 2019

- [1] M. Shinohara, K. Sabra, J. L. Gennisson, M. Fink, M. L. Tanter, *Muscle Nerve* **2010**, *42*, 438.
- [2] K. Khanafer, A. Duprey, M. Schlicht, R. Berguer, *Biomed. Microdevices* **2009**, *11*, 503.
- [3] C. Cipriani, F. Zaccone, S. Micera, M. C. Carrozza, *IEEE Trans. Rob.* **2008**, *24*, 170.
- [4] J. Gomez-Gil, I. San-Jose-Gonzalez, L. F. Nicolas-Alonso, S. Alonso-Garcia, *Sensors* **2011**, *11*, 7110.
- [5] D. Tkach, H. Huang, T. A. Kuiken, *J. NeuroEng. Rehabil.* **2010**, *7*, 21.
- [6] R. Merletti, A. Botter, A. Troiano, E. Merlo, M. Alessandro, *Clin. Biomech.* **2009**, *24*, 122.
- [7] M. Abdoli-Eramaki, C. Damecour, J. Christenson, J. Stevenson, *J. Electromyogr. Kinesiol.* **2012**, *22*, 908.
- [8] P. Morel, E. Ferrea, B. Taghizadeh-Sarshouri, J. M. C. Audí, R. Ruff, K. P. Hoffmann, S. Lewis, M. Russold, H. Dietl, L. Abu-Saleh, D. Schroeder, W. Krautschneider, T. Meiners, A. Gail, *J. Neural Eng.* **2016**, *13*, 016002.
- [9] J. M. Hahne, D. Farina, N. Jiang, D. Liebetanz, *Front. Neurosci.* **2016**, *10*, 114.
- [10] N. Matsuhisa, M. Kaltenbrunner, T. Yokota, H. Jinno, K. Kuribara, T. Sekitani, T. Someya, *Nat. Commun.* **2015**, *6*, 7461.

- [11] K. Nagamine, S. Chihara, H. Kai, H. Kaji, M. Nishizawa, *Sens. Actuators, B* **2016**, 237, 49.
- [12] S. Budday, R. Nay, R. de Rooij, P. Steinmann, T. Wyrobek, T. C. Ovaert, E. Kuhl, *J. Mech. Behav. Biomed. Mater.* **2015**, 46, 318.
- [13] M. Zhang, H. Liu, P. Cao, B. Chen, J. Hu, Y. Chen, B. Pan, J. A. Fan, R. Li, L. Zhang, Y. Su, *J. Appl. Mech. ASME* **2017**, 84, 121010.
- [14] Y. Y. Hsu, M. Gonzalez, F. Bossuyt, F. Axisa, J. Vanfleteren, I. De Wolf, *J. Mater. Res.* **2009**, 24, 3573.
- [15] Y. Y. Hsu, M. Gonzalez, F. Bossuyt, F. Axisa, J. Vanfleteren, I. De Wolf, *Thin Solid Films* **2011**, 519, 2225.
- [16] K. I. Jang, H. N. Jung, J. W. Lee, S. Xu, Y. H. Liu, Y. Ma, J. W. Jeong, Y. M. Song, J. Kim, B. H. Kim, A. Banks, J. W. Kwak, Y. Yang, D. Shi, Z. Wei, X. Feng, U. Paik, Y. Huang, R. Ghaffari, J. A. Rogers, *Adv. Funct. Mater.* **2016**, 26, 7281.
- [17] M. Wade, Y.-C. Li, G. M. Wahl, *Nat. Rev. Cancer* **2013**, 13, 83.
- [18] Y. Morikawa, S. Yamagiwa, H. Sawahata, R. Numano, K. Koida, M. Ishida, T. Kawano, *Adv. Healthcare Mater.* **2018**, 7, 1701100.
- [19] J. Park, S. Choi, A. H. Janardhan, S. Y. Lee, S. Raut, J. Soares, K. Shin, S. Yang, C. Lee, K. W. Kang, H. R. Cho, S. J. Kim, P. Seo, W. Hyun, S. Jung, H. J. Lee, N. Lee, S. H. Choi, M. Sacks, N. Lu, M. E. Josephson, T. Hyeon, D. H. Kim, H. J. Hwang, *Sci. Transl. Med.* **2016**, 8, 344ra86.
- [20] S. Wagner, S. Bauer, *MRS Bull.* **2012**, 37, 207.
- [21] K. Tybrandt, D. Khodagholy, B. Dielacher, F. Stauffer, A. F. Renz, *Adv. Mater.* **2018**, 30, 1706520.
- [22] Y. Morikawa, S. Yamagiwa, H. Sawahata, M. Ishida, T. Kawano, in *2016 IEEE 29th Int. Conf. Micro Electro Mech. Syst.*, IEEE, Piscataway, NJ **2016**, pp. 149–152.
- [23] S. Yamagiwa, M. Ishida, T. Kawano, in *IEEE 26th Int. Conf. Micro Electro Mech. Syst.*, IEEE, Piscataway, NJ **2013**, pp. 480–483.
- [24] S. Yamagiwa, M. Ishida, T. Kawano, *Appl. Phys. Lett.* **2015**, 107, 083502.
- [25] M. Ochoa, P. Wei, A. J. Wolley, K. J. Otto, B. Ziaie, *Biomed. Microdevices* **2013**, 15, 437.
- [26] B. J. Raiteri, A. G. Cresswell, G. A. Lichtwark, *PeerJ* **2016**, 4, e2260.
- [27] D.-H. Kim, J. Viventi, J. J. Amsden, J. Xiao, L. Vigeland, Y.-S. Kim, J. A. Blanco, B. Panilaitis, E. S. Frechette, D. Contreras, D. L. Kaplan, F. G. Omenetto, Y. Huang, K.-C. Hwang, M. R. Zakin, B. Litt, J. A. Rogers, *Nat. Mater.* **2010**, 9, 511.
- [28] R. M. Palmieri, C. D. Ingersoll, M. A. Hoffman, *J. Athl. Train.* **2004**, 39, 268.
- [29] H. Steffens, P. Dibaj, E. D. Schomburg, *Physiol. Res.* **2012**, 61, 203.
- [30] B. Katz, R. Miledi, *Proc. R. Soc. London, Ser. B* **1965**, 161, 483.
- [31] M. J. Wayner, R. Emmers, *Am. J. Physiol.* **1958**, 194, 403.
- [32] A. M. Tan, S. Chakrabarty, H. Kimura, J. H. Martin, *J. Neurosci.* **2012**, 32, 12896.
- [33] C. C. Smith, R. W. P. Kissane, S. Chakrabarty, *eNeuro* **2018**, 5, ENEURO.0227.
- [34] R. Sun, S. C. Carreira, Y. Chen, C. Xiang, L. Xu, B. Zhang, M. Chen, I. Farrow, F. Scarpa, J. Rossiter, *Adv. Mater. Technol.* **2019**, 4, 1900100.
- [35] R. Zhao, S. Lin, H. Yuk, X. Zhao, *Soft Matter* **2018**, 14, 2515.
- [36] Y. Cho, J.-H. Shin, A. Costa, T. A. Kim, V. Kunin, J. Li, S. Y. Lee, S. Yang, H. N. Han, I.-S. Choi, D. J. Srolovitz, *Proc. Natl. Acad. Sci. USA* **2014**, 111, 17390.
- [37] E. Dirren, J. Aebischer, C. Rochat, C. Towne, B. L. Schneider, P. Aebischer, *Ann. Clin. Transl. Neurol.* **2015**, 2, 167.
- [38] S. Yamagiwa, A. Fujishiro, H. Sawahata, R. Numano, M. Ishida, T. Kawano, *Sens. Actuators, B* **2015**, 206, 205.
- [39] S. Venkatraman, J. Hendricks, Z. A. King, A. J. Sereno, S. Richardson-Burns, D. Martin, J. M. Carmena, *IEEE Trans. Neural Syst. Rehabil. Eng.* **2011**, 19, 307.
- [40] C. Ethier, E. R. Oby, M. J. Bauman, L. E. Miller, *Nature* **2012**, 485, 368.
- [41] B. D. Farnsworth, D. M. Talyor, R. J. Triolo, D. J. Young, in *Proc. TRANSDUCERS 2009 – 15th Int. Conf. Solid-State Sensors, Actuators Microsystems*, IEEE, Piscataway, NJ **2009**, pp. 358–361.